# Optical study of electronic structure and electron-phonon coupling in $ZrB_{12}$

J. Teyssier, A. B. Kuzmenko, D. van der Marel, and F. Marsiglio
*Département de Physique de la Matière Condensée, Université de Genève, Quai Ernest-Ansermet 24, 1211 Genève 4, Switzerland*

A. B. Liashchenko, N. Shitsevalova, and V. Filippov
*Institute for Problems of Materials Science, National Academy of Sciences of Ukraine, 252680 Kiev, Ukraine*

(Received 18 September 2006; revised manuscript received 22 December 2006; published 4 April 2007)

We report the optical (6 meV–4 eV) properties of a boride superconductor $ZrB_{12}$ ($T_c$=6 K) in the normal state from 20 to 300 K measured on high-quality single crystals by a combination of reflectivity and ellipsometry. The Drude plasma frequency and interband optical conductivity calculated by the self-consistent, full-potential linear muffin-tin orbital method agree well with experimental data. The Eliashberg function $\alpha^2_{tr}F(\omega)$ extracted from optical spectra features two peaks at about 25 and 80 meV, in agreement with specific heat data. The total coupling constant is $\lambda_{tr}=1.0\pm0.35$. The low-energy peak presumably corresponds to the displacement mode of Zr inside $B_{24}$ cages, while the second one involves largely boron atoms. In addition to the usual narrowing of the Drude peak with cooling down, we observed an unexpected removal of about 10% of the Drude spectral weight, which was partially transferred to the region of the lowest-energy interband transition (~1 eV). This effect may be caused by the delocalization of the metal ion from the center of the $B_{24}$ cluster.

DOI: 10.1103/PhysRevB.75.134503 PACS number(s): 74.70.Ad, 78.20.Ci, 78.30.−j

## I. INTRODUCTION

Boron, like carbon, covalently bonds to itself, easily forming rigid three-dimensional clusters and networks as well as planes, chains, and even nanotubes. The discovery of superconductivity in graphitelike $MgB_2$ at 40 K (Ref. 1) has stimulated intense research on other superconducting boron phases, which have, however, so far shown quite modest transition temperatures. Zirconium dodecaboride $ZrB_{12}$ has one of the highest known $T_c \approx 6$ K among the binary borides except $MgB_2$. Even though its superconductivity was discovered almost 40 years ago,[2] only recent progress in single-crystal growth has enabled extensive studies on it.

In dodecaborides $MB_{12}$, boron atoms make up a three-dimensional network forming spacious $B_{24}$ cages which accommodate metal ions. The isotope effect in $ZrB_{12}$ for zirconium[3] ($\beta \approx -0.32$) is much larger than for boron[4] ($\beta \approx -0.09$), pointing to a large contribution of lattice modes involving Zr atoms to the electron-phonon coupling responsible for superconductivity in $ZrB_{12}$. The inversion of specific heat measurements[5] creates a pronounced peak in the phonon density of states at about 15 meV, attributed to Zr vibrations in oversized boron cages. The coupling to this mode can also be enhanced by strong anharmonicity. The contribution to the electron-phonon coupling of this mode has also been reported in Seebeck effect measurements.[6]

Notably, significant controversy exists regarding the strength of the electron-phonon interaction. According to the McMillan formula, a weak-to-medium coupling $\lambda \approx 0.68$ provides the observed $T_c$, given the phonon mode frequency of 15 meV and a "standard" value of the screened Coulomb potential $\mu^* \approx 0.1-0.15$.[7] A weak coupling was confirmed by specific heat measurements.[5] However, tunneling[8] and point-contact spectroscopy[7] yield $2\Delta_0/k_BT_c \approx 4.8$, suggesting a very strong coupling regime. This discrepancy between the results of surface and bulk probes has been ascribed to the surface-enhanced superconductivity in $ZrB_{12}$.[8,9] A two band gap model has also been proposed to account for unusual magnetic penetration depth and upper critical field temperature dependencies.[10] In principle, the value of $\lambda$ can also be derived from the dc resistivity measurements, although this calculation relies on the unknown value of the plasma frequency.

Band-structure calculation[11] shows that B $2p$ and Zr $4d$ states contribute almost equally to the density of states at the Fermi level. This makes $ZrB_{12}$ electronically very different from $MgB_2$, where Mg states have a vanishing contribution to the metallic and superconducting properties.[12] However, no experiments which can directly verify the prediction of the band theory, such as those using angle-resolved photoemission (ARPES) and de Haas–van Alphen (dHvA) effect, have been done so far on this compound.

Optical spectroscopy, which probes free-carrier charge dynamics and provides experimental access to plasma frequency, electron scattering, and interband transitions, may help clarify a number of existing uncertainties and test the predictions of the band calculations. By a combination of reflectivity and ellipsometry, we have obtained spectra of optical conductivity and dielectric function in the broad range of photon energies and frequencies. We have concentrated on general optical fingerprints of the electronic structure of $ZrB_{12}$ in the normal state.

For comparison, we have performed calculations of the band structure and corresponding optical properties. The electron-phonon coupling function $\alpha^2_{tr}F(\omega)$ has been extracted from the fit of optical data and compared with thermodynamic and Raman measurements.

An unusual decrease of the Drude plasma frequency with cooling down has been observed. By comparing $ZrB_{12}$ with other clustered compounds, we have found that the delocalization of the metal ion (weakly bonded to the boron network) from the center of the boron cage could be at the origin of large changes in the electronic properties.

 

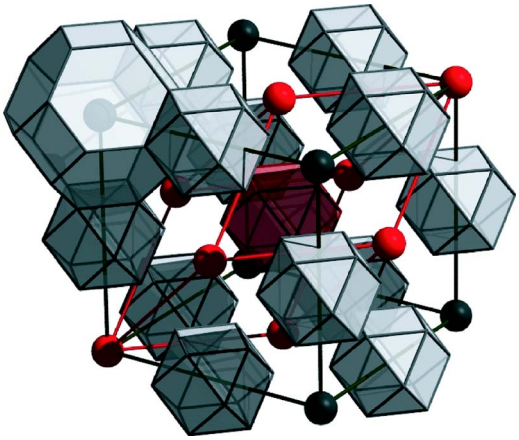

FIG. 1. (Color online) Crystal structure of $ZrB_{12}$. The clusters $B_{12}$ and $B_{24}$ are displayed as polyhedrons. The unit cell containing 13 atoms is colored in red.

## II. CRYSTAL STRUCTURE

$ZrB_{12}$ crystallizes in the $UB_{12}$-type structure,[13] which can be viewed as a cubic rocksalt arrangement of Zr and $B_{12}$ cuboctahedral clusters (Fig. 1). For our discussion, it may be more convenient to represent this structure as a face-centered-cubic structure of Zr surrounded by $B_{24}$ cages.

## III. OPTICAL EXPERIMENT AND RESULTS

Large single crystals of $ZrB_{12}$ were grown using a high-frequency induction zone furnace.[14] Optical measurements were performed on a (001) surface with dimensions of 4 $\times 4$ mm$^2$. The surface of this extremely hard material was polished using diamond abrasive disks with the finest grain size of 0.1 $\mu$m. In the photon energy range of 0.8–4 eV, the complex dielectric function $\epsilon(\omega)$ was determined directly using spectroscopic ellipsometry at an incident angle of 60°. For photon energies between 6 meV and 0.8 eV, the reflectivity of the sample was measured using a Bruker 113 Fourier transform infrared spectrometer. For both ellipsometry and reflectivity experiments, the sample was mounted in a helium flow cryostat allowing measurements from room temperature down to 7 K. The reference was taken by *in situ* gold evaporation.

Figure 2(a) presents the real and imaginary parts of $\epsilon(\omega)$ measured by ellipsometry at selected temperatures. The reflectivity measured at low frequencies and extracted from the dielectric constant in the visible range are plotted in Fig. 2(b).

In order to obtain the optical conductivity in the infrared region, we used a variational routine[15] yielding the Kramers-Kronig consistent dielectric function which reproduces all the fine details of the infrared reflectivity data while *simultaneously* fitting to the complex dielectric function in the visible and UV range. This procedure anchors the phase of the infrared reflectivity to the phase at high energies measured with ellipsometry.[16]

Figure 3(a) shows the evolution of the optical conductivity with temperature. One can see a Drude-type peak that

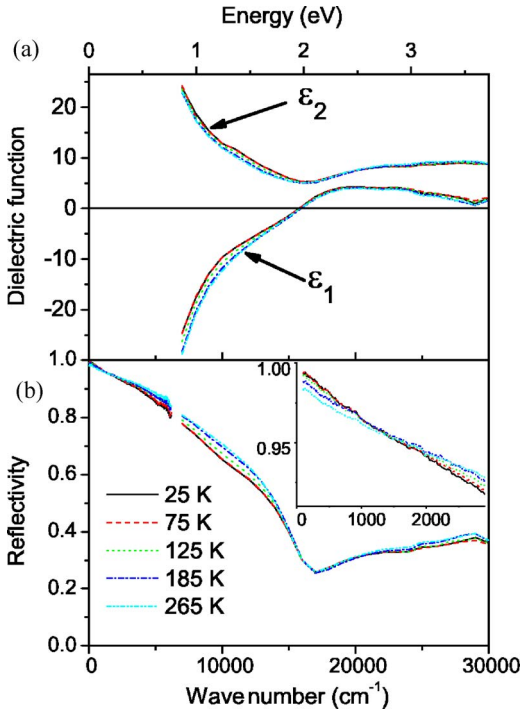


FIG. 2. (Color online) (a) Real and imaginary parts of the dielectric function measured by ellipsometry. (b) Reflectivity measured in the infrared and calculated from the dielectric constant at higher frequencies. Inset: low-frequency region.

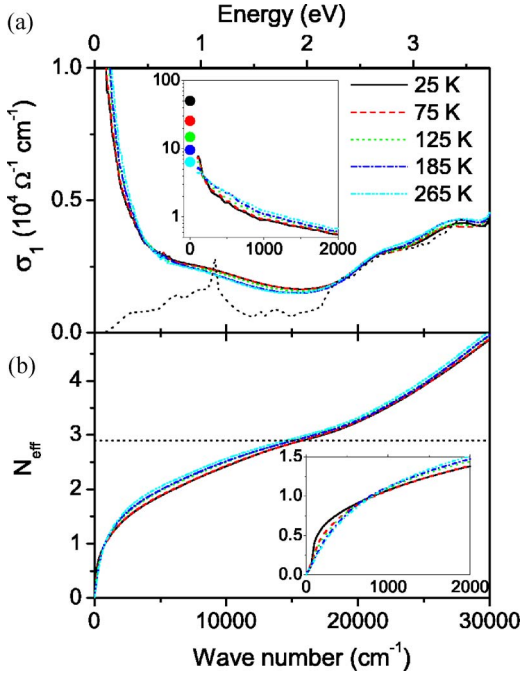


FIG. 3. (Color online) (a) Optical conductivity of $ZrB_{12}$ at selected temperatures. Inset: low-energy part; symbols represent $\sigma_{dc}$ from Ref. 7. The dotted line shows the interband conductivity from LDA calculation. (b) Effective number of carriers per unit cell of 13 atoms. Inset: low-frequency part; the horizontal dotted line corresponds to the calculated plasma frequency of 6.3 eV.

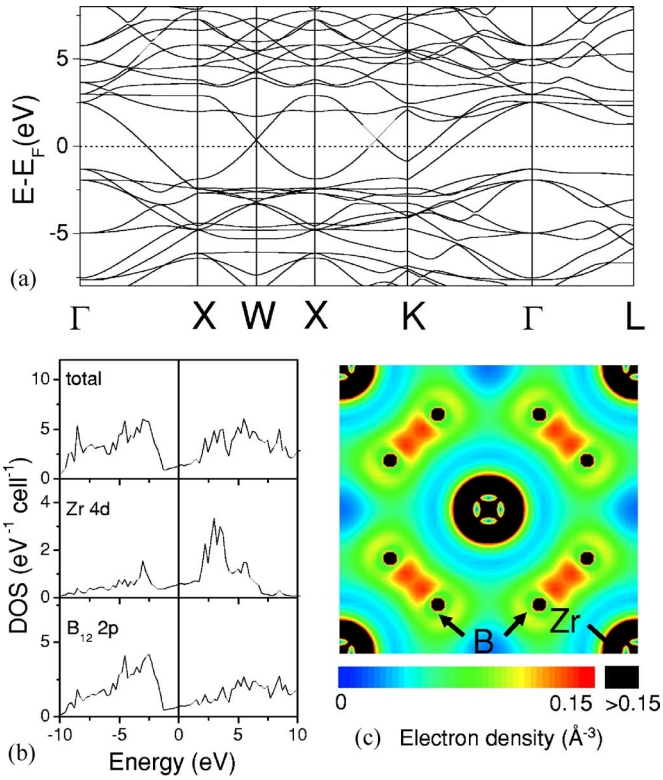


FIG. 4. (Color online) (a) Calculated band structure. (b) Partial density of states (PDOS) of $ZrB_{12}$. (c) Charge density in the *a-b* plane of the cubic cell.

indicates a metallic behavior. The dc conductivity ($\sigma_{dc}$) (Refs. 5 and 7) plotted as symbols in the inset of Fig. 3(a) agrees reasonably well with the extrapolation of the optical data to zero frequency.

Figure 3(b) depicts the effective number of carriers,

$$N_{\text{eff}}(\omega) = \frac{2mV_c}{\pi e^2}\int_0^{\omega} \sigma_1(\omega')d\omega', \tag{1}$$

where $m$ is the free electron mass, $e$ is the electron charge, and $V_c = 101.5$ Å$^3$ is the unit cell volume. We have observed a transfer of spectral weight to low energy, which comes from the narrowing of the Drude peak. For higher energies (above 100 meV), an unusual decrease of up to 10% has been observed. This will be discussed in Sec. V C.

## IV. LOCAL-DENSITY APPROXIMATION CALCULATIONS

### A. Band structure

The band structure of the unit cell containing 13 atoms was calculated. We used a full-potential plane-wave linear muffin-tin orbital (LMTO) program[17] within a local spin-density approximation (LSDA) and a generalized gradient approximation (GGA).[18] The band structure for high-symmetry directions in the Brillouin zone (BZ) is shown in Fig. 4(a). The density of states (DOS) calculated by the tetrahedron method is displayed in Fig. 4(b). It appears clearly that the main contribution to the DOS at the Fermi level comes from zirconium 4*d* and boron 2*p* states. The total

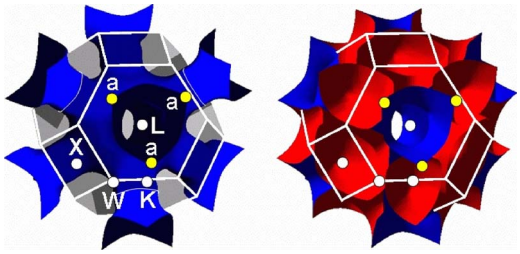


FIG. 5. (Color online) Fermi surface of $ZrB_{12}$ containing two sheets: a holelike network (blue) and electronlike closed surfaces (red). In the left figure, only the first sheet is displayed for clarity. The points of tangential contact between the two sheets are designated by the symbol *a*.

DOS at the Fermi level $N(E_F) = 1.59$ eV$^{-1}$ cell$^{-1}$. The $N(E_F)$ for a zirconium *d* electron is 0.55 eV$^{-1}$ cell$^{-1}$ and the one for *p* electrons of $B_{12}$ clusters is 0.65 eV$^{-1}$ cell$^{-1}$, which is in good agreement with a previous report.[11]

Mapping the repartition of charges in a crystal is helpful in understanding the chemical bonding. The calculated charge density of valence electrons in the *a-b* plane of the cubic cell is displayed in Fig. 4(c). The high density between direct neighbor boron atoms indicates a strong covalent bonding while the ion in the middle of the $B_{24}$ cage (Zr in our case) is weakly bonded to the boron skeleton. This has strong consequences on vibration modes in the crystal and may explain the presence of a very low-frequency phonon (~15 meV) associated with a displacement of the zirconium atom in the $B_{24}$ cage.

Figure 5(a) shows the Fermi surface in the first Brillouin zone. The sheet centered at *X* (marked in red in Fig. 5) has an electron character, while the network centered on the Γ point (marked in blue in Fig. 5) is of a hole character. The two sheets touch at point *a* along the Γ-*X* direction. In contrast to $MgB_2$, which exhibits a strongly anisotropic Fermi surface composed of different sheets with carriers of a very different character, the Fermi surface in $ZrB_{12}$ is much more isotropic.

### B. Optical properties

The local-density approximation (LDA) band structure allows us to calculate the optical parameters. The interband contribution to the real part of the optical conductivity can be deduced from the equation

$$\sigma_1(\omega) = \frac{e^2}{12\pi^2 m^2 \omega}\sum_{f,i}\int_{\text{BZ}} d^3k |P_{fi}|^2 \delta[E_f(k) - E_i(k) - \hbar\omega],$$

$$P_{fi} = \frac{\hbar}{i}\langle f|\nabla|i\rangle.$$

Here, $E_i(k)$ and $E_f(k)$ are the energies of the initial (occupied) and final (empty) states, respectively. $k$ is the wave vector inside the BZ where the transition $E_i(k) \rightarrow E_f(k)$ occurs. Only direct transitions are taken into account. The calculated optical conductivity is shown as the dotted line in Fig. 3(a), together with experimental curves. At frequencies above 2 eV, a very good agreement is observed. At lower

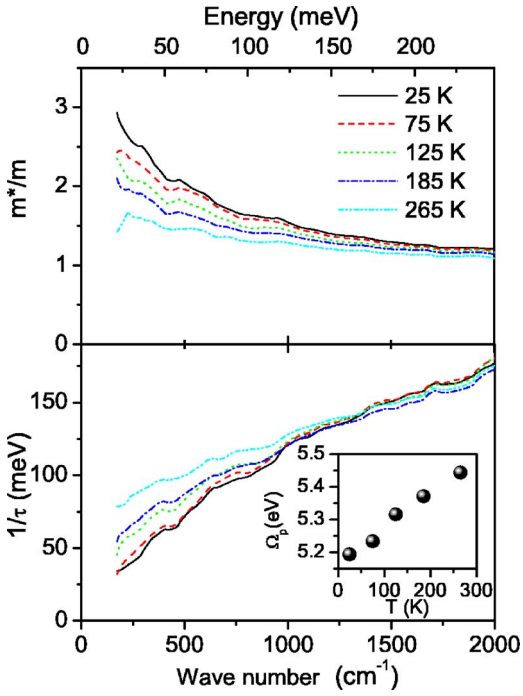


FIG. 6. (Color online) Extended Drude analysis of the optical conductivity of $ZrB_{12}$ for different temperatures. Inset shows the $T$ dependence of the plasma frequency used to calculate $m^*/m$ and $1/\tau$.

frequencies, the experimental curves are systematically higher, likely due to the tail of the Drude peak.

The plasma frequency was computed through integration on the Fermi surface,

$$\Omega_{p,\mathrm{LDA}}^2 = \frac{e^2}{12\pi^2}\int_{FS} v_f\, dS, \tag{2}$$

where $v_f$ is the Fermi velocity. We found a value $\Omega_{p,\mathrm{LDA}} = 6.3$ eV which corresponds to $N_{\mathrm{eff}} \approx 2.9$ [dotted line in Fig. 3(b)]. The experimental value of $N_{\mathrm{eff}}(\omega)$ reaches this level at about 2 eV where the experimental optical conductivity [Fig. 3(a)] shows a minimum. This indicates that the calculated plasma frequency is close to the experimental one.

## V. ANALYSIS AND DISCUSSION

### A. Extended Drude analysis

Figure 6 shows the frequency dependence of the mass renormalization $m^*(\omega)/m_b$ (where $m_b$ is the band mass) and the scattering rate $1/\tau(\omega)$ obtained by the extended Drude formalism,

$$\frac{m^*(\omega)}{m_b} = -\frac{\Omega_p^2}{4\pi\omega}\,\mathrm{Im}\left[\frac{1}{\sigma(\omega)}\right], \tag{3}$$

$$\frac{1}{\tau(\omega)} = \frac{\Omega_p^2}{4\pi}\,\mathrm{Re}\left[\frac{1}{\sigma(\omega)}\right]. \tag{4}$$

The plasma frequency $\Omega_p$ was obtained at each temperature by the integration of optical conductivity from 0 to 0.74 eV (6000 $\mathrm{cm}^{-1}$) (inset in Fig. 6). This cutoff frequency was chosen such that $\Omega_p$ is close to the plasma frequency obtained using the fitting procedure (fit 3) described below. The temperature dependence of $\Omega_p$ is too large to be neglected as is usually done.

At low frequencies, the decrease of the scattering rate with cooling down indicates a narrowing of the Drude peak. The strong frequency dependence below 100 meV of $1/\tau(\omega)$ and $m^*(\omega)/m_b$ indicates a significant electron-boson (presumably electron-phonon) interaction.

### B. Electron-phonon coupling

The signature of an electron-phonon interaction shown by the extended Drude analysis makes the simple Drude model inapplicable in describing the low-frequency region. Therefore, we adopted the following model for the dielectric function:

$$\epsilon(\omega) = \epsilon_\infty - \frac{\Omega_p^2}{\omega[\omega + iM(\omega,T)]} + \sum_j \frac{\Omega_{p,j}^2}{\omega_{0,j}^2 - \omega^2 - i\omega\gamma_j}, \tag{5}$$

where $\epsilon_\infty$ represents the contribution of core electrons, and the second and third terms describe free carriers and interband contributions, respectively. The latter is taken to be a sum of Lorentzians with adjustable parameters. The frequency-dependent scattering of the free carriers is expressed via the memory function,

$$M(\omega,T) = \gamma_{\mathrm{imp}} - 2i\int_0^\infty d\Omega\, \alpha_{\mathrm{tr}}^2 F(\Omega) K\left(\frac{\omega}{2\pi T}, \frac{\Omega}{2\pi T}\right), \tag{6}$$

where $\gamma_{\mathrm{imp}}$ is the impurity scattering rate and $\alpha_{\mathrm{tr}}^2 F(\Omega)$ is the transport Eliashberg function. The kernel $K$ is[19]

$$K(x,y) = \frac{i}{y} + \left\{\frac{y-x}{x}[\Psi(1-ix+iy) - \Psi(1+iy)]\right\} - \{y \to -y\}, \tag{7}$$

where $\Psi(x)$ is the digamma function.

The reflectivity at normal incidence is

$$R(\omega) = \left|\frac{\sqrt{\epsilon(\omega)} - 1}{\sqrt{\epsilon(\omega)} + 1}\right|^2. \tag{8}$$

We fit simultaneously $R(\omega)$ at low frequencies and both $\epsilon_1(\omega)$ and $\epsilon_2(\omega)$ at high frequencies.

As a starting point, we used $\alpha^2 F(\Omega)$ deduced from specific heat and resistivity measurements [neglecting the difference between isotropic $\alpha^2 F(\Omega)$ and transport $\alpha_{\mathrm{tr}}^2 F(\Omega)$] (Ref. 5) and adjusted all other parameters [fit 1: solid red curve in Fig. 7(a)]. This function (solid curve in Fig. 8) has two peaks at around 12 and 60 meV and gives $\lambda = 0.68$. A clear improvement of the fit quality was achieved compared to one with a single Drude peak (dashed dotted curve) with a frequency-independent scattering rate. The reflectivity curve is within absolute reflectivity error bars of 0.5%. This means that optical data are consistent with the mentioned value of the coupling constant and the observed $T_c$.[5,7]

It is also important to determine the spread of parameters consistent with optical data alone. It is known that the ex-

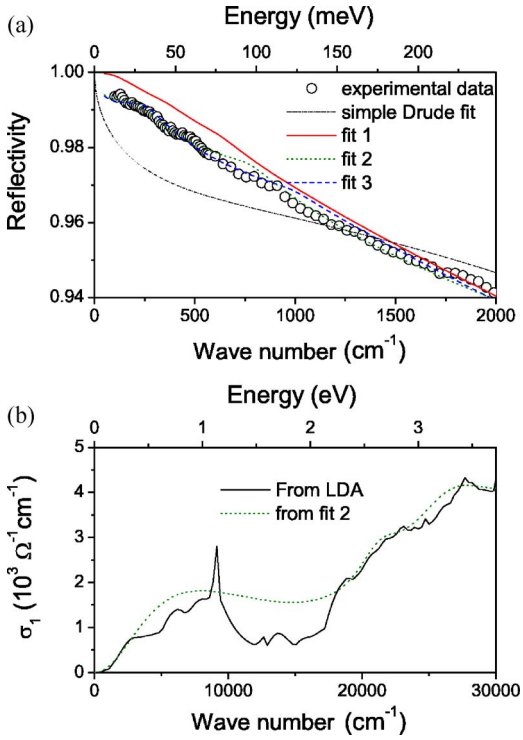


FIG. 7. (Color online) (a) Different fits of reflectivity at 25 K. The dash-dotted line is a fit with a single Drude peak. Fit 1 with $\alpha^2F(\Omega)$ is from Ref. 5 (solid red curve). Fits 2 and 3 with $\alpha^2_{tr}F(\Omega)$ are adjustable as described in the text. (b) Interband contribution to optical conductivity calculated from LDA (solid curve) and obtained from fit 3 as described in the text.

traction of $\alpha^2F(\Omega)$ from optical data is an ill-posed problem,[20–22] which means that fine details cannot be extracted. We model the Eliashberg function as a superposition of Dirac peaks,

$$\alpha^2_{tr}F(\Omega) = \sum_k A_k \delta(\Omega - x_k), \tag{9}$$

and treat $A_k$ and $x_k$ as free parameters. We did not succeed in obtaining a reasonable fit with a single mode even using

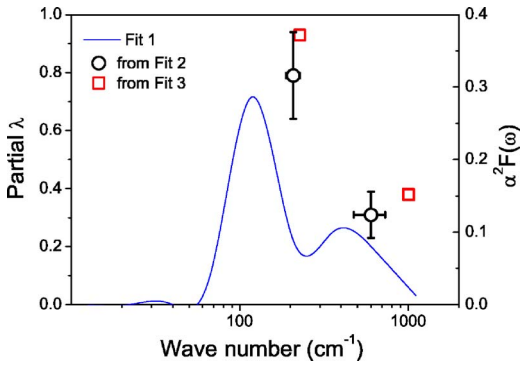


FIG. 8. (Color online) The solid curve (fit 1) corresponds to $\alpha^2F(\Omega)$ from Ref. 5. Central phonon frequencies and partial coupling constant extracted from the fit of optical data with fit 2 (cicles) and fit 3 (squares) procedures as described in the text.

TABLE I. Set of parameters used in fits 2 and 3. In fit 3, the Lorentzian $L_1$ is split into three different ones.

| | | Fit 2 | Fit 3 | | |
|---|---|---|---|---|---|
| $\epsilon_\infty$ | | 3.33 | 3.28 | | |
| $\Omega_p$ (eV) | | 5.5 | 5.2 | | |
| $\gamma_{imp}$ (meV) | | 33 | 28 | | |
| | | | $L_{1a}$ | $L_{1b}$ | $L_{1c}$ |
| Low energy ($L_1$) | $\omega_o$ (eV) | 1 | 0.32 | 0.74 | 1.21 |
| | $\Omega_p$ (eV) | 4.6 | 1.03 | 0.50 | 5.76 |
| | $\gamma$ (eV) | 1.8 | 0.30 | 0.15 | 2.75 |
| $L_2$ | $\omega_o$ (eV) | 2.6 | | 2.8 | |
| | $\Omega_p$ (eV) | 1.9 | | 2.1 | |
| | $\gamma$ (eV) | 0.6 | | 0.5 | |
| $L_3$ | $\omega_o$ (eV) | 3.3 | | 3.4 | |
| | $\Omega_p$ (eV) | 4.7 | | 4.1 | |
| | $\gamma$ (eV) | 1.3 | | 1.0 | |
| $L_4$ | $\omega_o$ (eV) | 4.8 | | 4.7 | |
| | $\Omega_p$ (eV) | 8.3 | | 7.9 | |
| | $\gamma$ (eV) | 1.9 | | 1.6 | |

some Gaussian broadening within 10 meV, but two peaks are sufficient to reproduce the shape of experimental curves. The central frequencies were found to be $x_1 = 208 \pm 19$ cm$^{-1}$ and $x_2 = 602 \pm 128$ cm$^{-1}$. The weights are $A_1 = 83 \pm 21$ cm$^{-1}$ and $A_2 = 94 \pm 35$ cm$^{-1}$, respectively. The electron-phonon coupling constant can be derived from the parameters of the fit by the relation

$$\lambda_{tr} = 2\int_0^\infty \frac{d\Omega\ \alpha^2_{tr}F(\Omega)}{\Omega} = 2\sum_k \frac{A_k}{x_k}. \tag{10}$$

In our case, this ratio leads to a partial coupling constant $\lambda_{tr,1} = 0.82 \pm 0.28$ for the mode at $x_1$ and $\lambda_{tr,2} = 0.18 \pm 0.10$ for the mode at $x_2$. The total $\lambda_{tr} = 1.00 \pm 0.35$. The other parameters of the fit are displayed in Table I. The reflectivity corresponding to this fit (fit 2) is displayed as the dotted (green) curve in Fig. 7(a).

The low-frequency mode can be logically assigned to the vibration of weakly bonded zirconium ions inside $B_{24}$ cages, although the *ab initio* calculation of the phonon structure is needed to substantiate this assignment. The high-frequency mode presumably corresponds to a rigid boron network vibration, a situation similar to that of intercalated fullerenes and other clustered covalent structures.

The error bars of $x_k$ and $A_k$ are quite large because of a significant numerical fit correlation between the lowest-energy interband transition and the parameters of the oscillator ($L1$ in Table I) and those of $\alpha^2_{tr}F(\Omega)$. In other words, it is difficult to decouple the effects of a low-energy interband transition and an electron-phonon interaction on the optical conductivity. Therefore, we performed another fit (fit 3) where the interband contribution was modeled (parameters in

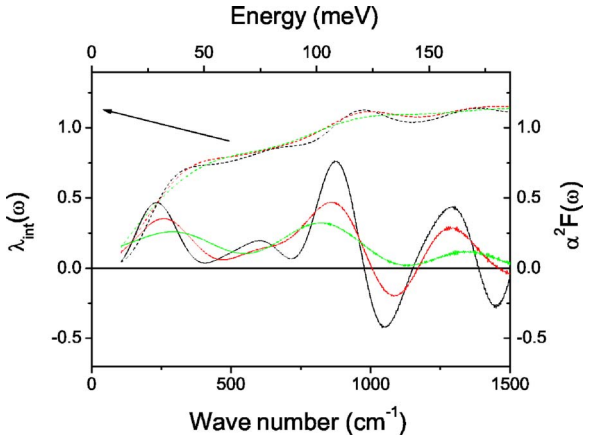


FIG. 9. (Color online) $\alpha_{tr}^2F(\Omega)$ obtained using Eq. (11) at $T=25$ K (solid curves) and integrated coupling constant $\lambda_{tr,int}(\omega)$ (dashed curves) for different smoothening windows.

Table I) to match that of the interband optical conductivity calculated by LDA [solid line in Fig. 7(b)]. The presence of sharp structures slightly worsens the quality of the fit. The low-energy mode of $\alpha_{tr}^2F(\Omega)$ is almost unchanged by this procedure ($x_1=227$ cm$^{-1}$, $A_1=106$ cm$^{-1}$, and $\lambda_{tr1}=0.93$) but the second mode tends to shift to higher frequencies ($x_2=1003$ cm$^{-1}$, $A_2=190$ cm$^{-1}$, and $\lambda_{tr2}=0.38$) and the total coupling constant becomes $\lambda_{tr}=1.3$. The reflectivity corresponding to fit 3 is plotted as a dashed blue curve in Fig. 7(a).

The central frequencies $x_k$ and partial electron-phonon constants $\lambda_k$ are shown as symbols in Fig. 8 for fit 2 (circles) and fit 3 (squares) described above. The Eliashberg function from Ref. 5 used in fit 1 is plotted as a solid curve. Central frequencies of the phonons are larger than those derived from specific heat and resistivity measurements[5] (140 and 420 cm$^{-1}$) (Fig. 8).

A more traditional way to extract $\alpha_{tr}^2F(\Omega)$ from optical conductivity is to directly use the inversion formula,[20,23]

$$\alpha_{tr}^2F(\omega)=\frac{1}{2\pi}\frac{\Omega_p^2}{4\pi}\frac{d^2}{d\omega^2}\left[\omega\,\mathrm{Re}\,\frac{1}{\sigma(\omega)}\right]. \tag{11}$$

One can also calculate the integrated coupling constant,

$$\lambda_{tr,int}(\omega)=2\int_0^{\omega}\frac{d\Omega\;\alpha_{tr}^2F(\Omega)}{\Omega}. \tag{12}$$

Taking the frequency derivative twice requires heavy spectral smoothening of optical data. The result of inversion is given in Fig. 9 for different frequency smoothening windows. The robust features in $\alpha_{tr}^2F(\omega)$ are the peaks at about 250 and 900 cm$^{-1}$, in good agreement with the results obtained by fitting procedures described above. Since Eq. (11) assumes the absence of a low-energy interband transition, in our case some spurious features in $\alpha_{tr}^2F(\omega)$ may appear at frequencies above $\sim$1000 cm$^{-1}$. Even though smoothening has a significant influence on the shape of $\alpha_{tr}^2F(\omega)$, all curves $\lambda_{tr,int}(\omega)$ lie almost on top of each other and give a value of about 1.1 around 1000 cm$^{-1}$. Summarizing the results of all

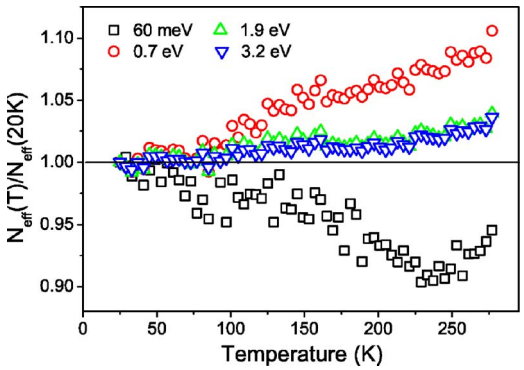


FIG. 10. (Color online) Temperature dependence of relative effective number of carriers for different cutoff energies.

previously described approaches to extract $\alpha_{tr}^2F(\omega)$, we obtained $\lambda_{tr}=1.0\pm0.3$. This value indicates a medium to strong coupling in $ZrB_{12}$.

### C. Temperature dependence of Drude spectral weight

The plasma frequency $\Omega_p$ at 25 K, obtained from different fits (Table I), is 5.2–5.5 eV. The uncertainty comes from the fact that interband contributions can not be separated unambiguously from the Drude peak. This value is slightly lower than that calculated by LDA (6.3 eV). However, this agreement is good and it suggests that LDA describes well the conduction bands near the Fermi surface. The temperature dependence of the plasma frequency appears anomalous though. As mentioned above, the integrated number of carriers decreases for energies above 100 meV when the temperature is decreased. This is shown in Fig. 10 where we plot $N_{\mathrm{eff}}$ as a function of temperature normalized by its value at 20 K for selected cutoff frequencies. The effect is maximal (about 10%) at around 0.7 eV. Normally, the narrowing of the Drude peak with a temperature-independent plasma frequency results in a slight (1%–2%) increase of $N_{\mathrm{eff}}$ at frequencies of 0.5–1 eV. In our case one has to assume that the plasma frequency decreases with cooling down. On the other hand, spectral weight is almost recovered at around 2 eV, which is due to the fact that it is transferred from the low-frequency range to the region between 0.5 and 2 eV (Fig. 3).

We do not have a definitive explanation for this effect. In order to check the direct effect of temperature on the band structure, we have performed LDA calculations at finite temperatures by adding a Fermi-Dirac distribution to the bands filling in the self-consistent calculation. The thermal expansion was also taken into account using data from Ref. 5. We found that the calculated plasma frequency decreases by around 0.4% with increasing temperature from 0 to 600 K. Both the sign and the amplitude of the change in the calculated plasma frequency cannot explain the experimental observations. The spectral weight due to interband transitions has also been calculated and found to be almost temperature independent. Therefore, a decrease of 10% in the spectral weight is so big that it likely results from a significant change in the electronic band structure.

One can speculate that a certain structural instability is due to the ability of zirconium atoms to move almost freely

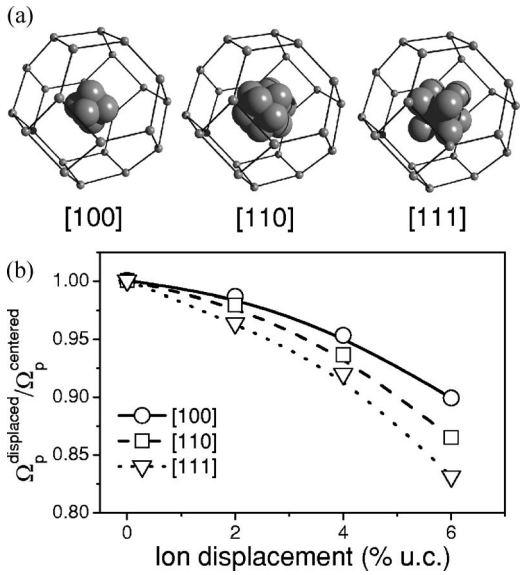


FIG. 11. (a) Representation of displacement directions in the $B_{24}$ cage. (b) Plasma frequency versus ionic displacement along the [100], [110], and [111] directions.

in spacious boron cages. According to Ref. 24, a displacement of the metal ion in the $B_{24}$ cage of about 5% of the unit cell is responsible for the symmetry breaking, which makes the low-frequency Zr mode Raman active. We have therefore calculated the band structure and the plasma frequency as a function of displacement of the metal ion in the directions [100], [110], and [111]. The delocalization configurations are sketched in Fig. 11(a).

Electron states at the Fermi surface come equally from Zr atoms and the $B_{12}$ cluster [Fig. 4(b)]. Therefore, the highest plasma frequency is obtained when the Zr ion is in the center of the $B_{24}$ cluster. The plasma frequency decrease will be more pronounced when Zr shifts toward a region with lower charge density [Fig. 11(b)].

Such an anomalously large atomic displacement has already been observed in clathrate-type systems that present a similar cluster structure.[25,26] In these compounds, the displacement of an ion located in the middle of a cage is strongly anisotropic and can be described by a fractionally occupied split site. It was also found that this atomic disorder was present from room temperature down to 10 K.

In the picture of a multiple well potential, the delocalization due to thermal excitation tends to center the ion in the cage. At low temperature, the ion is located in the bottom of the well out of the central position. Further structural investigations are necessary to elucidate the relevancy of this or other scenarios in dodecaborides. This kind of spectral weight transfer is also predicted by models where the charge carriers are small polarons.[27] While keeping in mind that these have been derived for a low charge carrier density, the observed direction of the spectral weight transfer agrees with those models.

## VI. CONCLUSIONS

In this work, optical properties of zirconium dodecaboride have been studied as a function of temperature. We found that LDA theory predicts correctly interband optical conductivity and free electron plasma frequency.

$ZrB_{12}$ appears to be a good metal with a bare plasma frequency of about 5.5 eV. The Eliashberg function $\alpha_{tr}^2F(\Omega)$ was extracted by two methods giving consistent results. Two peaks were found in $\alpha_{tr}^2F(\Omega)$ at about 200 and 1000 $cm^{-1}$, which is consistent with specific heat measurements.[5] A medium to high electron-phonon coupling regime was found with $\lambda_{tr} \simeq 1.0$ in agreement with a high ratio $2\Delta_o/kT_c=4.8$ from tunneling measurements.[8] The low-frequency peak that likely corresponds to a vibration mode of zirconium in boron cages is the main contributor to the coupling constant.

However, this compound shows deviations from conventional metallic behavior. Namely, a significant anomaly in the temperature evolution of the integrated spectral weight was observed. About 10% of the spectral weight was removed from the Drude peak and transferred to the region of low-energy interband transitions. The origin of this anomaly has not been clearly identified. However, our simulation of the impact of the delocalization of the metal ion in the boron cages shows that this could be responsible for the large change in the plasma frequency.

## ACKNOWLEDGMENTS

The authors would like to thank Rolf Lortz and Alain Junod for fruitful exchanges. We also gratefully acknowledge interesting discussions with V. A. Gasparov. This work was supported by the Swiss National Science Foundation through Grant No. 200020-109588 and the National Center of Competence in Research (NCCR) "Materials with Novel Electronic Properties-MaNEP". F.M. greatly appreciates the hospitality of the Department of Condensed Matter Physics at the University of Geneva. This work was supported in part by the Natural Sciences and Engineering Research Council of Canada (NSERC), by ICORE (Alberta), and by the Canadian Institute for Advanced Research (CIAR).

[1] J. Nagamatsu, N. Nakagawa, T. Muranaka, Y. Zenitani, and J. Akimitsu, Nature (London) **410**, 63 (2001).
[2] B. T. Matthias, T. H. Geballe, K. Andres, E. Corenzwit, G. W. Hull, and J. P. Maita, Science **159**, 530 (1968).
[3] C. W. Chu and H. H. Hill, Science **159**, 1227 (1968).
[4] Z. Fisk, A. C. Lawson, B. T. Matthias, and E. Corenzwit, Phys. Lett. **37A**, 251 (1971).
[5] R. Lortz, Y. Wang, S. Abe, C. Meingast, Yu. B. Paderno, V. Filippov, and A. Junod, Phys. Rev. B **72**, 024547 (2005).
[6] V. Glushkov, M. Ignatov, S. Demishev, V. Filippov, K. Flachbart, T. Ishchenko, A. Kuznetsov, N. Samarin, N. Shitsevalova, and N. Sluchanko, Phys. Status Solidi B **243**, 72 (2006).

[7] D. Daghero, R. S. Gonnelli, G. A. Ummarino, A. Calzolari, V. Dellarocca, V. A. Stepanov, V. B. Filippov, and Y. B. Paderno, Supercond. Sci. Technol. **17**, 250 (2004).
[8] M. I. Tsindlekht, G. I. Leviev, I. Asulin, A. Sharoni, O. Millo, I. Felner, Yu. B. Paderno, V. B. Filippov, and M. A. Belogolovskii, Phys. Rev. B **69**, 212508 (2004).
[9] R. Khasanov, D. Di Castro, M. Belogolovskii, Yu. Paderno, V. Filippov, R. Brütsch, and H. Keller, Phys. Rev. B **72**, 224509 (2005).
[10] V. A. Gasparov, N. S. Sidorov, and I. I. Zver'kova, Phys. Rev. B **73**, 094510 (2006).
[11] I. R. Shein and A. L. Ivanovskii, Phys. Solid State **45**, 1429 (2003).
[12] J. Kortus, I. I. Mazin, K. D. Belashchenko, V. P. Antropov, and L. L. Boyer, Phys. Rev. Lett. **86**, 4656 (2001).
[13] A. Leithe-Jasper, A. Sato, and T. Tanaka, Z. Kristallogr. **217**, 319 (2002).
[14] Y. B. Paderno, A. B. Liashchenko, V. B. Filippov, and A. V. Dukhnenko, Proceedings of the International Conference on Science for Materials in the Frontier of the Centuries: Advantages and Challenges, IPMS NASU, Kiev, 2002 (unpublished), p. 347.
[15] A. B. Kuzmenko, Rev. Sci. Instrum. **76**, 083108 (2005).
[16] I. Bozovic, Phys. Rev. B **42**, 1969 (1990).
[17] S. Y. Savrasov, Phys. Rev. B **54**, 16470 (1996).
[18] J. P. Perdew, K. Burke, and M. Ernzerhof, Phys. Rev. Lett. **77**, 3865 (1996).
[19] O. Dolgov and S. Shulga, J. Supercond. **8**, 611 (1995).
[20] F. Marsiglio, J. Supercond. **12**, 163 (1999).
[21] S. Shulga, cond-mat/0101243 (unpublished).
[22] S. V. Dordevic, C. C. Homes, J. J. Tu, T. Valla, M. Strongin, P. D. Johnson, G. D. Gu, and D. N. Basov, Phys. Rev. B **71**, 104529 (2005).
[23] F. Marsiglio, T. Startseva, and J. Carbotte, Phys. Lett. A **245**, 172 (1998).
[24] H. Werheit, Y. Paderno, V. Filippov, V. Paderno, A. Pietraszko, M. Armbrüster, and U. Schwarz, J. Solid State Chem. (to be published).
[25] B. Chakoumakos, B. Sales, D. Mandrus, and G. Nolas, J. Alloys Compd. **296**, 80 (2000).
[26] B. Chakoumakos, B. Sales, and D. Mandrus, J. Alloys Compd. **322**, 127 (2001).
[27] D. Emin, Phys. Rev. B **48**, 13691 (1993).